Tidal Mixing Events on the Deep Flanks of Kaena Ridge, Hawaii

JEROME AUCAN, MARK A. MERRIFIELD, DOUGLAS S. LUTHER, AND PIERRE FLAMENT

Department of Oceanography, University of Hawaii at Manoa, Honolulu, Hawaii

(Manuscript received 20 September 2004, in final form 7 September 2005)

ABSTRACT

A 3-month mooring deployment (August–November 2002) was made in 2425-m depth, on the south flank of Kaena Ridge, Hawaii, to examine tidal variations within 200 m of the steeply sloping bottom. Horizontal currents and vertical displacements, inferred from temperature fluctuations, are dominated by the semidiurnal internal tide with amplitudes of ≥ 0.1 m s^{-1} and $\sim$100 m, respectively. A series of temperature sensors detected tidally driven overturns with vertical scales of $\sim$100 m. A Thorpe scale analysis of the overturns yields a time-averaged dissipation near the bottom of 1.2×10^{-8} W kg^{-1}, 10–100 times that at similar depths in the ocean interior 50 km from the ridge. Dissipation events much larger than the overall mean (up to 10^{-6} W kg^{-1}) occur predominantly during two phases of the semidiurnal tide: 1) at peak downslope flows when the tidal stratification is minimum ($N = 5 \times 10^{-4}$ s^{-1}) and 2) at the flow reversal from downslope to upslope flow when the tidal stratification is ordinarily increasing ($N = 10^{-3}$ s^{-1}). Dissipation associated with flow reversal mixing is 2 times that of downslope flow mixing. Although the overturn events occur at these tidal phases and they exhibit a general spring–neap modulation, they are not as regular as the tidal currents. Shear instabilities, particularly due to tidal strain enhancements, appear to trigger downslope flow mixing. Convective instabilities are proposed as the cause for flow reversal mixing, owing to the oblique propagation of the internal tide down the slope. The generation of similar tidally driven mixing features on continental slopes has been attributed to oblique wave propagation in previous studies. Because the mechanical energy source for mixing is primarily due to the internal tide rather than the surface tide, the observed intermittency of overturn events is attributed to the broadbanded nature of the internal tide.

1. Introduction

Deep-ocean diapycnal mixing is an important but poorly understood component of the general ocean circulation. One common viewpoint of the thermohaline circulation is that dense water sinks at high latitudes, spreads throughout the ocean interior, and returns to the surface in regions of upwelling. Munk (1966) speculated that this upward advection of cold water is balanced by a mechanically driven downward diffusion of heat, resulting in the observed stratification below the main thermocline. The amount of diapycnal mixing necessary to maintain abyssal stratification was estimated by Munk (1966) and later by Munk and Wunsch (1998) to be equivalent to a global-averaged eddy diffusivity of $K_\rho = 10^{-4}$ m^2 s^{-1}. Decades of direct turbulence measurements in the open ocean have failed to find much more than one-tenth of this value (Gregg 1991). Munk (1966) had also suggested that the required global average might be dominated by intense mixing in localized regions near topography. This idea has been refined with theory and observations, beginning with Armi (1978, 1979). It is now known that diapycnal mixing below the thermocline is strongly dependent on location, being largest in the vicinity of rough seafloor topography (Kunze and Toole 1997; Toole et al. 1997; Polzin et al. 1997). The locations of the diapycnal mixing may determine the structure of the deep-ocean circulation (Samelson 1998; Hasumi and Suginohara 1999; Simmons et al. 2004). It can then be argued that a better knowledge of the spatial and temporal variations of mixing is paramount to a better understanding of the world's ocean circulation and its impact on climate (Rahmstorf 2003).

When turbulent mixing in a stratified layer occurs along a sloping boundary, mixed fluid is exported from the boundary layer to the interior, and undisturbed stratified fluid is incorporated into the boundary layer (Phillips et al. 1986; Garrett 1991). The mixed water, but not the turbulence itself, can then spread laterally

Corresponding author address: Jerome Aucan, University of Hawaii at Manoa, 1000 Pope Road, Honolulu, HI 96822.
E-mail: jaucan@soest.hawaii.edu

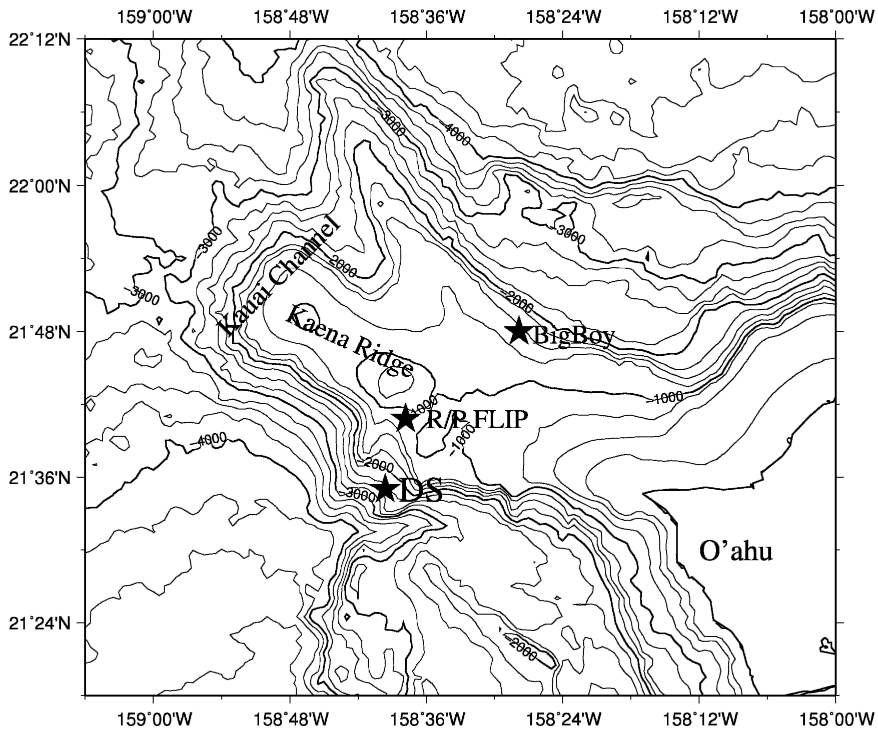

FIG. 1. Bathymetric map of the Kaena Ridge showing the locations of the DS mooring (this study), the Big Boy mooring (Levine and Boyd 2006), and R/P *FLIP* (Rainville and Pinkel 2006).

(e.g., via stirring by mesoscale variability) along neutral surfaces into the ocean's interior (Munk and Wunsch 1998). Enhanced mixing can also occur outside the boundary layer, although still within the neighborhood of the boundary, engendered by enhanced shear and strain from internal waves propagating outward from boundary sources. Although less relevant for our study, the reflection of incident internal waves can cause enhanced mixing along near-critical slopes (Eriksen 1998; Nash et al. 2004).

Mechanical energy can be supplied to deep boundary layers by a variety of processes, including large-scale and localized currents (Gross et al. 1986; Lukas et al. 2000) and/or a wide range of interactions between internal waves and topography [see Thorpe (1999) for a review]. The challenge is to document the mixing associated with these processes along sloping boundaries and ultimately to parameterize their effects in circulation models. In this regard, the tide is both an important source of mechanical energy, believed to be comparable to the surface wind stress (Wunsch 2000), and, because of its inherent predictability, a good candidate for parameterization. Recent studies have demonstrated the link between turbulent mixing and tidal processes [New and Pingree (1990) and Lien and Gregg (2001) among others]. Furthermore, Egbert and Ray (2000) estimate that 25%–30% of barotropic tidal dissipation occurs in the open ocean, primarily through the generation of internal tides.

It is now well established from various in situ and remote observations that energetic semidiurnal internal tides originate from the Hawaiian Ridge (Ray and Mitchum 1996; Dushaw et al. 1995). The Hawaii Ocean Mixing Experiment (HOME) was designed to investigate the details of the tidal dissipation along the Hawaiian chain. As part of the HOME modeling effort, the Princeton Ocean Model (POM) has been used to simulate barotropic-to-baroclinic tidal energy conversion at Kaena Ridge in the Kauai Channel (Fig. 1). The simulations show internal tide energy originating on each side of the ridge near the crest (Merrifield et al. 2006). The energy propagates along internal wave characteristics: one beam propagates up and away from the ridge, a second propagates up and over the ridge, and a third propagates downward along the ridge flank when there is either a near- or supercritical slope below the generation site (Fig. 2). Energy dissipated by this downgoing beam as it propagates along the ridge flank is available for turbulent mixing at the slope. The numerical model (Merrifield and Holloway 2002) indicates an M_2 baroclinic energy flux of ~10 GW radiating away from the entire Hawaiian Ridge. Klymak et al. (2006), using direct dissipation measurements from four different instru-

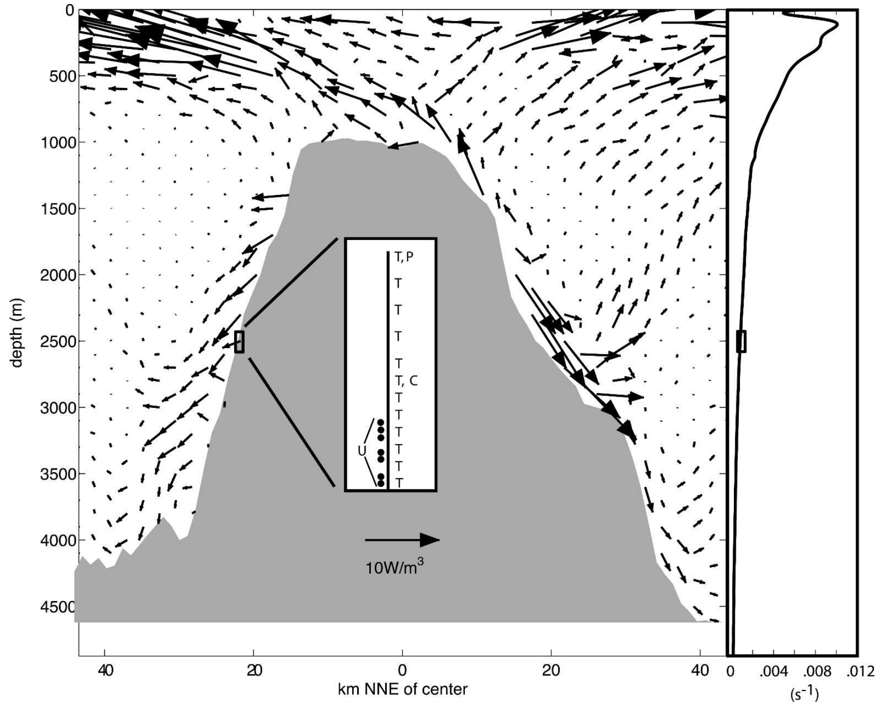

FIG. 2. A cross section of the ridge, in the approximate location of DS, showing estimates of M_2 baroclinic energy flux from Merrifield and Holloway (2002). The mooring is located in the path of a downgoing tidal beam. The stratification profile (right) is from a nearby CTD station occupied during the mooring deployment. The small inset (drawn to scale) shows the mooring location, and the larger inset shows the location on the mooring line of temperature (T) and current (C) measurements.

ments, estimate 7 ± 3 GW of turbulent dissipation along the entire Hawaiian Ridge. The tidally generated component of this net dissipation remains to be determined.

To complement the sparse temporal resolution of HOME microstructure measurements near the bottom, deep moorings were deployed near the ridge top and over the flanks of Kaena Ridge between the islands of Oahu and Kauai. These moorings were designed to sample temperature and current over the first hundreds of meters above the bottom. Indirect estimates of dissipation can be obtained through detection and analysis of turbulent overturns. Levine and Boyd (2006) deployed such a mooring near the ridge top (1450 m) on the northern flank and found significant overturns linked to tidal phase and amplitude. Levine and Boyd (2006) describe a scenario in which the internal tide first strains the mean density field, leading to regions of low buoyancy frequency N that subsequently overturn. The phase of the tide when overturns occur varies with depth. They found an average dissipation level of $\sim 10^{-8}$ W kg^{-1} for the entire experiment. Similar levels of dissipation near the bottom have been reported in direct microstructure measurements (Klymak et al. 2006).

In this paper we examine temperature and current data from a deep (2425 m) mooring on the southern flank of Kaena Ridge. We use estimates of dissipation based on a Thorpe scale analysis to show that mixing associated with the semidiurnal internal tide is vigorous at this depth (dissipation events $\geq 10^{-7}$ W kg^{-1}). The time series provide a unique view of deep mixing driven by a tidal current. The paper is organized as follows. The mooring location and instrumentation are first described in section 2. The observed flow characteristics are discussed in section 3 along with the convention we used to assign semidiurnal phases to the time series. The method for estimating turbulent overturns and the associated dissipation is described in section 4. In section 5 we identify two types of mixing events, related to different phases of the semidiurnal tide, and investigate their relationship with observed shear and strain. In section 6, we propose a generation mechanism for the most energetic type of mixing, based on the observation that the semidiurnal internal tide propagates obliquely relative to the slope. A discussion and summary follow in section 7.

2. Experiment site and data collection

Mooring DS was deployed on the south flank of Kaena Ridge near the 2425-m isobath (Figs. 1 and 2). At this location, the average buoyancy frequency is 0.001 s^{-1}, and the typical bottom slope is between 1/4 and 1/5. In comparison, the characteristic slope for an M_2 frequency internal wave is between 1/7 and 1/8. The topographic gradient is oriented at 35° relative to true north. The deployment lasted 87 days between 16 August and 11 November 2002. Swath bathymetry maps (resolution 150 m) show that the mooring was located in a slight depression between two ridges running down the slope and separated by ~10 km. Bottom roughness on scales shorter than 150 m was not determined.

Numerical model simulations indicate that semidiurnal frequency internal tides are generated near the 1000-m isobath along this portion of the Kaena Ridge (Merrifield and Holloway 2002). From here, a portion of the energy takes the form of a downward-propagating tidal beam (Fig. 2). This feature has been observed in microprofiler and expendable current profiler data by Nash et al. (2006) and Lee et al. (2006). The mooring was positioned in the path of the downgoing beam.

The mooring included an upward-looking RD Instruments (RDI) 300-kHz ADCP, 22 m above the bottom (mab) with a nominal range of approximately 100 m. The ADCP data are 8-min averages with a vertical resolution of 4 m. The acoustic return from some depth bins was contaminated by the sidelobe reflection off the mooring elements, which biases the current speed toward zero. These bins were not used in the analysis, although the data are included in some figures for reference. Reliable current estimates (~0.02 m s^{-2} for an 8-min-averaged sample) were obtained out to a range of only 40–60 m, presumably because of a low concentration of acoustic scatterers at this depth.

Sea-Bird Electronics temperature sensors (SBE 39) recorded 3-min averages. The sensors were located between 25 and 220 mab, with sensor spacing varying between 16 and 24 m. The accuracy and resolution of the sensor are 2×10^{-3}°C and 10^{-4}°C, respectively. For the detection of density inversions it is important to account for any bias errors in the measurements. Averaged over the 3 months of the experiment, temperatures show slight departures from a linear depth profile (Fig. 3a). Because tidal motions induce isotherm displacements of 200 m peak to peak past the mooring sensors, we assume that the sensors sample water with similar properties, so the departures from a smooth linear profile are taken to be instrument bias errors. We therefore calculate corrections for each of the sensors so that the 3-month-averaged vertical profile is linear. We checked for differential sensor drift over time by repeating the corrections based on monthly averages. The results are similar to the 3-month time average, suggesting that differential drift errors are not an important factor. (The impact of these corrections on overturn detection is discussed in section 4.)

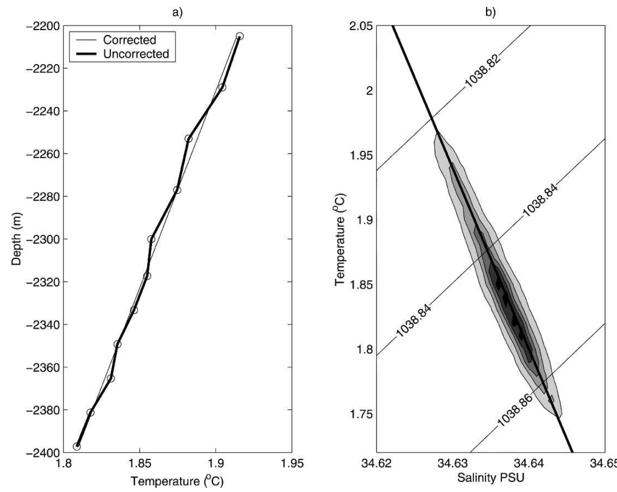

FIG. 3. (a) Temperatures averaged over the entire deployment show small departures from a linear profile, which are interpreted as instrument bias errors. (b) The distribution of temperature and salinity measured at 2317-m depth, 107 m above the bottom (mab). The black line is a linear fit of the data.

The sensors at 107 mab provide a collocated measure of temperature and salinity. We find that temperature and salinity are described adequately by a linear relation at this depth (Fig. 3b). Given the range of vertical displacements observed at the sensors, we assume that this relation applies over the 200-m depth range of the mooring. The salinity at the location of the other sensors is therefore estimated from the linear T–S relation and the potential temperature (calculated for a reference pressure equal to that of the temperature–conductivity sensor). Potential density is calculated for all sensors using the same reference pressure. Potential density is used for overturn detection.

3. Current and temperature variability

Time series of current and temperature sampled near the bottom are dominated by fluctuations at semidiurnal frequency (Fig. 4). Temperature changes ≥0.3°C occur during spring tides and ≤0.1°C during neap tides. The horizontal current is stronger in the across-slope direction than along slope with peak speeds of 0.2 m s^{-1}

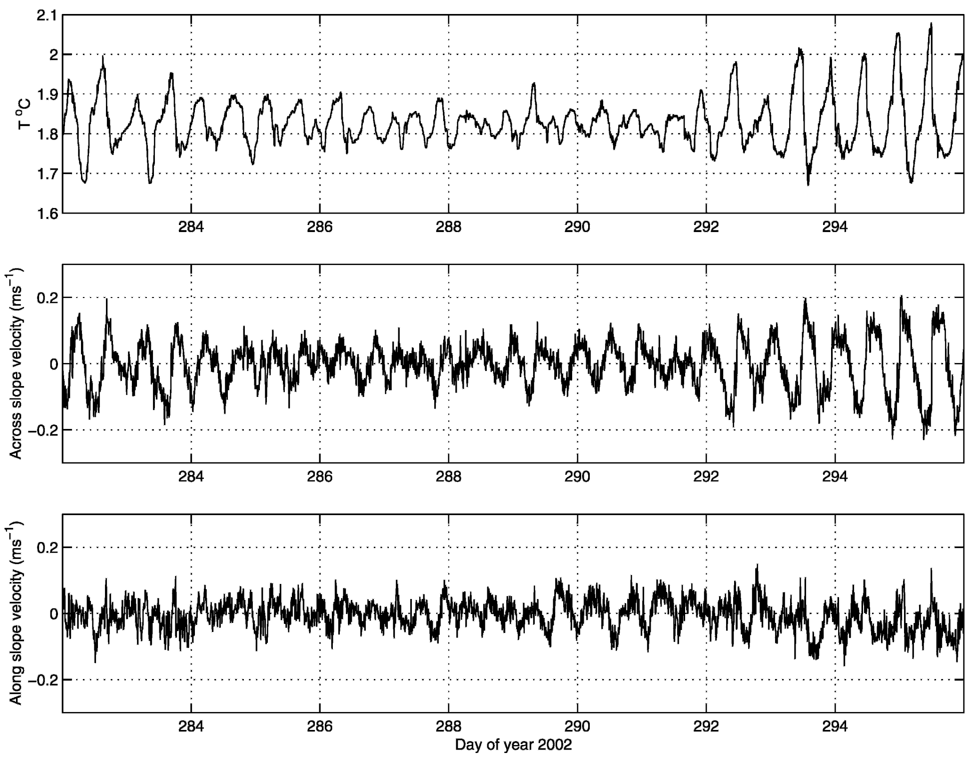

FIG. 4. A representative 14-day time series of temperature (75 mab) and across-slope and along-slope currents (65 mab).

during springs and <0.1 m s^{-1} during neaps. The along-slope flow is typically <0.1 m s^{-1}, although the ratio of across-slope to along-slope varies over the course of the experiment because of changes in the baroclinic tidal component.

Spectra of horizontal velocity, shear, and buoyancy frequency all show peak energy at the semidiurnal frequency band (Fig. 5). Spectral peaks at the diurnal and inertial frequency bands are noticeably smaller than the semidiurnal peak. The semidiurnal band accounts for 60% of the total current variance at each depth, with the M_2 constituent alone accounting for 50% of the variance. Similar ratios are found for vertical shear and temperature. A standard tidal analysis (Foreman 1978) confirms that the semidiurnal constituents are approximately an order of magnitude larger than the diurnal (Table 1). In general, the M_2 and weaker S_2 constituents create a fortnightly spring–neap cycle (up to a factor-of-4 difference in current amplitude).

The current ellipses for the dominant M_2 tidal constituent are directed across the local isobaths (across ridge). The angle between the topographic gradient and the semimajor axis of the M_2 current ellipses varies between 15° and 30° over the depth range examined (Fig. 6). The semimajor axis of the M_2 current is ~0.07 m s^{-1} with similar ellipse structure between 45 and 65 mab (Fig. 6). Although the current amplitude of the other depth bins is suspect, we include them in Fig. 6 to show that the orientation and eccentricity of the current ellipses are similar over the depth range. The ellipses also tilt in the across-ridge/depth plane such that the across-ridge flow is parallel to the slope (not shown). Greenwich phases for the current ellipses range from 40° to 50°.

The M_2 barotropic current, predicted either by the POM simulations (Merrifield and Holloway 2002) or the TPXO model (Egbert 1997), is out of phase with the measured semidiurnal current (Fig. 6). When the semidiurnal surface elevation is high over the ridge, barotropic currents are directed southwestward (Merrifield and Holloway 2002). At this phase of the tide, baroclinic currents along the south flank nearly oppose the barotropic current in model simulations (Merrifield and Holloway 2002) in agreement with the observed current (Fig. 6). This is due to the dominance of the baroclinic tidal current over the barotropic tidal current at these depths. This leads us to conclude that the dominant energy source for tidal motions at the mooring location is the baroclinic component of the tide. A more thorough model–data comparison of near-bottom currents at the DS site will be considered in a later study using a higher-resolution model grid (currently 1–4 km).

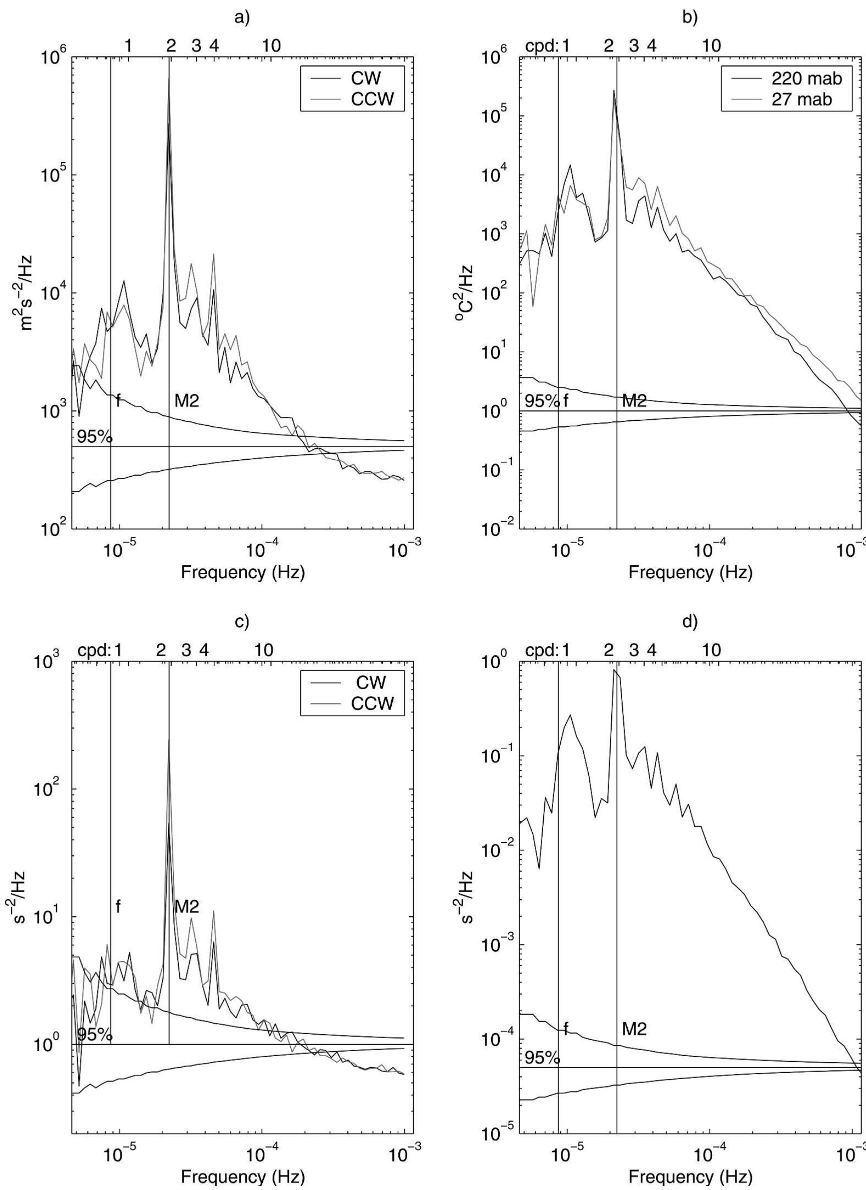

FIG. 5. Power spectra of (a) horizontal current at 65 mab, (b) temperature (220 and 27 mab), (c) vertical shear of the horizontal current (between 40 and 65 mab), and (d) depth-averaged buoyancy frequency (27–220 mab). Top abscissa is in cycles per day (cpd).

The observed temperature variations (Fig. 4) are due primarily to vertical advection of the background stratification by the semidiurnal tide, with maximum temperatures associated with maximum downward displacements. The M_2 temperature variations are converted to vertical displacements using the mean stratification profile obtained from a nearby CTD station. The resulting displacement amplitudes exceed 100 m at all depths, corresponding to 200-m peak-to-peak changes in isotherm depths over a 12.42-h cycle. Because of the proximity of the bottom boundary, these displacements include a lateral component up and down the slope. Vertical displacement phases show a small increase with distance from the bottom, indicating that displacements near the bottom lead displacements 200 m above the bottom by approximately 14° (30 min). Vertical displacements lag currents by 110°, close to the 90° difference expected for a freely propagating internal tide, and also consistent with the advection of stratified water up and down the slope.

The raw temperature time series are 3-min averages that are not aligned in time. We interpolate the data to

TABLE 1. Contribution of the main diurnal and semidiurnal tidal constituents to horizontal velocities at 65 mab and temperature at 60 mab.

	Tidal constituent					
	O_1	K_1	N_2	M_2	L_2	S_2
Velocity (m s^{-1})	0.0055	0.003	0.025	0.074	0.01	0.029
Greenwich phase (°)	341	286	83	52	324	89
Temperature ($\times 10^{-3}$°C)	7.1	2.2	27	63.5	4.6	14.2
Greenwich phase (°)	262	133	337	294	234	338

a common 3-min sample interval and compute potential density. The dataset is then treated as a series of vertical potential density profiles. Each potential density profile is interpolated by a spline function with 1-m resolution in the vertical, and unstable regions are detected with a tracking algorithm.

4. Turbulent overturns, Thorpe scales, and dissipation estimates

The mooring provides a time series of vertical temperature profiles. A noticeable feature of these profiles is the frequent occurrence of statically unstable patches, or turbulent overturns. Figures 7 and 8 show two examples of these overturns. In both cases, the temperature becomes nearly homogeneous over the 200-m depth range, followed by temperature inversions that affect the entire range. It is therefore impossible to assign a depth to these overturns, other than the middle of the sampled range. A temperature profile during the overturn shown in Fig. 8 illustrates the classic S-shaped inversion (Fig. 9). The inversion far exceeds the rated accuracy of the sensors. In Fig. 7, the water column slowly restratifies over the remainder of the tidal cycle. In Fig. 8, the overturning is followed by an abrupt drop in temperature near the boundary, suggestive of a thermal front or tidal bore, followed by a rapid restratification. We will show in section 5 that overturns tend to occur at the two tidal phases depicted in Figs. 7 and 8.

The detection and analysis of these turbulent overturns provides an estimate of mixing. Within each detected overturn of vertical size H, the unstable profiles are reordered into stable ones. Each sample ρ_n initially at a depth z_n is assigned a new depth z_m in the reordered profile. The difference $d'_n = z_m - z_n$ is called the Thorpe displacement (Thorpe 1977), and the Thorpe scale is defined as the root-mean-square of this quantity for each reordered overturn:

$$L_T = \overline{(d'^2)}^{1/2}. \tag{1}$$

The Thorpe scale can be related to another measure of turbulent dissipation, the Ozmidov length scale (Ozmidov 1965):

$$L_0 = \epsilon^{1/2} N^{-3/2}. \tag{2}$$

Several studies have shown a linear relationship between L_T and L_0 (Dillon 1982; Ferron et al. 1998). Dissipation can be estimated by

$$\epsilon = a^2 N^3 L_T^2, \tag{3}$$

where $a = L_0/L_T$. The value of a used in previous studies varies between 0.65 and 0.95 [see Finnigan et al. (2002) for a review]. For the sake of consistency with the mooring study of Levine and Boyd (2006), $a = 0.8$ in this analysis. Levine and Boyd also discuss the validity of the Thorpe scale method for estimating dissipation. In Eqs. (2) and (3), N is obtained from the reordered profile, and therefore is always real.

The smallest detectable overturn is determined by either the vertical spacing between adjacent sensors or the resolution of the sensors [see Finnigan et al. (2002) for more details]. At the depth range of interest, we estimate an average of 5.4×10^{-4}°C m^{-1} for $\partial T/\partial z$. The nominal accuracy of the instruments is 2×10^{-3}°C (Budeus and Schneider 1998), so the detection limit based on the sensor accuracy is 3.6 m, much smaller than the sensors spacing. The detection limit is therefore determined by the sensor spacing, which has an upper bound of 24 m. We identify overturns when their height exceeds this value. At the upper limit, overturns exceeding the spacing between the top and bottom sensors (200 m) are underestimated. Because a sizable number of the overturn events are characterized by inversions over the entire sample depth (i.e., Figs. 9 and 10), we consider our dissipation estimate to be a lower bound.

Of the 41 761 profiles analyzed, 14 700 or 34% contained at least one overturn >24 m. The correction applied to the temperature profile (see section 2) minimizes the detection of spurious overturns arising from sensor errors. For comparison, without the temperature correction, 23 000 profiles (or 54% of the total) contain at least one overturn > 24 m, but most of these overturns are associated with small temperature differences approaching the accuracy of the sensors (Fig. 10a). The

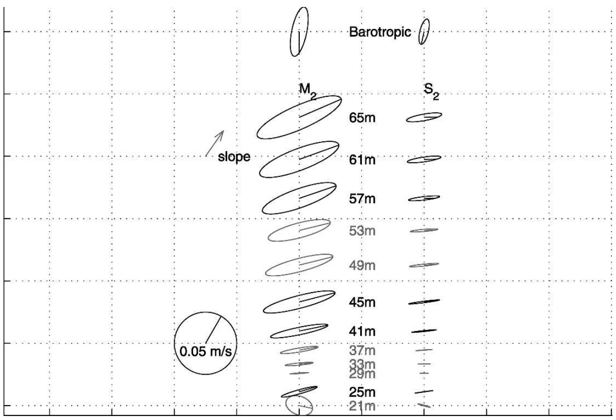

FIG. 6. The (left) M_2 and (right) S_2 measured horizontal current ellipses, with suspect depth bins in gray (i.e., sidelobe contamination problems). Barotropic current ellipses predicted by the TPXO model (Egbert 1997) are depicted at the top. The direction of the topographic gradient is indicated with the gray arrow on the left.

temperature correction also increases the mean size of small overturns and decreases the size of large overturns (Fig. 10b). The correction reduces the overall mean dissipation from 3.6×10^{-8} to 1.2×10^{-8} W kg^{-1}, while the large overturns are responsible for a relatively larger percentage of the dissipation (Fig. 10c).

Estimated Thorpe scales tend to be large (small) during spring (neap) tides (Fig. 11a). Thorpe scales range from 20 to 100 m for overturns of 24–190 m. For each detected overturn of size H_i, we calculate the dissipation ϵ_i using Eq. (3). For each profile, the average dissipation for the bottom layer is $\epsilon = H^{-1}\Sigma\epsilon_i H_i$, where $H = 200$ m. Dissipation values range from 10^{-7} to 10^{-6} W kg^{-1} during spring tides and from 10^{-8} to 10^{-7} W kg^{-1} during neap tides (Fig. 11b). The minimum attainable dissipation with this method is 1.2×10^{-10} W kg^{-1}. The time-averaged dissipation for this 200-m-thick layer is 1.2×10^{-8} W kg^{-1}. For comparison, Levine and Boyd (2006) found average dissipations of 10^{-8} W kg^{-1} for a 300-m-thick layer above the 1450-m isobath. Our average dissipation value should be treated with caution. Changes in the analysis method can lead to sizeable changes in the average. For example, a spline instead of a linear interpolation of the measurements leads to a 25% increase in the mean dissipation value. As already noted, the bias correction reduces the dissipation by 67%. We have attempted to make analysis choices that minimize the average dissipation.

Following Osborn (1980), we compute the vertical eddy diffusivity coefficient K_ρ by assuming that the turbulent kinetic energy balance is between shear production, buoyancy loss, and turbulent dissipation:

$$K_\rho = \Gamma\epsilon N^{-2}. \tag{4}$$

The mixing efficiency Γ is taken equal to 0.2, and N is now the background stratification. Converting the estimated dissipation values in this way, we obtain a time-averaged eddy diffusivity of 2×10^{-3} m^2 s^{-1}, two orders of magnitude higher than typical open-ocean estimates at this depth. For comparison, Klymak et al. (2006) found values of up to 10^{-2} m^2 s^{-1} near the ridge top, and Levine and Boyd (2006) found values of 10^{-3} m^2 s^{-1} near the bottom at their mooring site.

5. Dissipation events and the semidiurnal tide

Because the observations are dominated by oscillations at the M_2 frequency, we divide the time series into 163 M_2 cycles to investigate the mixing events in relation to tidal phase. A complex demodulation of the horizontal velocity is used to transform time into M_2 phase. With this convention, upslope flow occurs for phases between $-90°$ and $90°$ and downslope flow occurs during the rest of the cycle. We then ensemble average with respect to phase to obtain composites of temperature, velocity, and dissipation over the M_2 tidal cycle (Fig. 12).

Enhanced dissipation occurs during two distinct phases of the tidal cycle (shaded areas on Fig. 12). The first is centered around 140° and is associated with maximum downslope flows, increasing water temperatures, and low stratification. We refer to this mixing phase as "downslope flow mixing"; Fig. 7 is an example of a downslope flow-mixing event. The second peak, centered around $-90°$, is associated with the flow reversal from downslope to upslope, maximum water temperatures, and increasing stratification with a pronounced local minimum. We refer to this phase as "flow reversal mixing"; Fig. 8 is an example of a flow reversal mixing event.

Although observed mixing events are linked to tidal phase, they do not occur as regularly as the tide itself. To illustrate the variability of tidal mixing, we visually inspect each M_2 cycle and assign the cycle to one of five categories: "downslope flow mixing only" when dissipation occurs near the maximum downslope current; "flow reversal only" when dissipation occurs at the reversal from down to upslope flow; "both downslope flow mixing and flow reversal" when both events occur during the same cycle; "no mixing" when dissipation failed to reach a threshold value of 0.5×10^{-7} W kg^{-1}; and "random mixing event" when dissipation events occur at other phases of the tide. We find that 63% of the tidal cycles contain flow reversal and/or downslope flow mixing, 21% of the time series have no significant mixing, and 16% show only odd mixing events. Tidal cycles containing flow reversal mixing events account

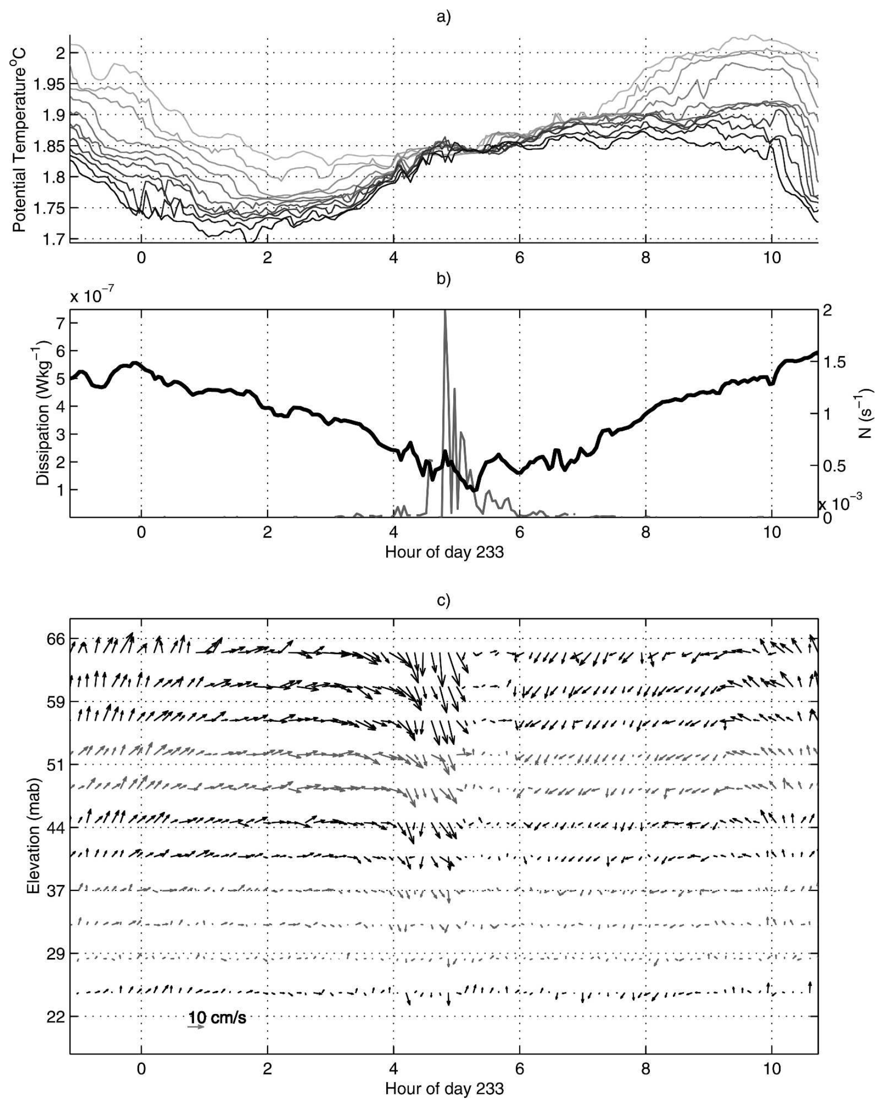

FIG. 7. A characteristic overturn event depicted in 12-h time series (day 233) of (a) potential temperature recorded at 27, 43, 59, 75, 91, 107, 124, 147, 171, 195, and 220 mab, with darker lines corresponding to smaller elevations above the bottom; (b) estimated dissipation [ϵ, Eq. (3), thin gray line] and depth-averaged buoyancy frequency (27–220 mab, thick black line); and (c) horizontal currents, rotated so that across-slope velocity is vertical. Depth bins with suspect sidelobe contamination are shown in gray.

for 40% of the total estimated dissipation, downslope flow events account for 20%, combined events 21%, and random events 16%. Although downslope flow mixing events appear throughout the experiment, flow reversal mixing events are nearly absent during the first spring–neap cycle, and their occurrence and amplitude appear to increase over time (Fig. 13a). We attribute this increase in part to the increase in semidiurnal current amplitude (Fig. 11). In addition, the first spring–neap cycle is characterized by more circularly polarized tidal currents than the other cycles (Fig. 13b). We will return to this point when considering the cause of flow reversal mixing events in section 6.

We next consider whether tidal shear and strain act to trigger mixing events, in the manner of shear instability. We calculate the shear over the depth range 41–65 mab. Again, the ADCP only samples a small fraction of the 200-m length of the thermistor chain. We also note that the shear over this depth range can represent a combination of boundary-flow-induced shear and turbulent shear from the overturns. The poor resolution of the current measurement does not allow for further

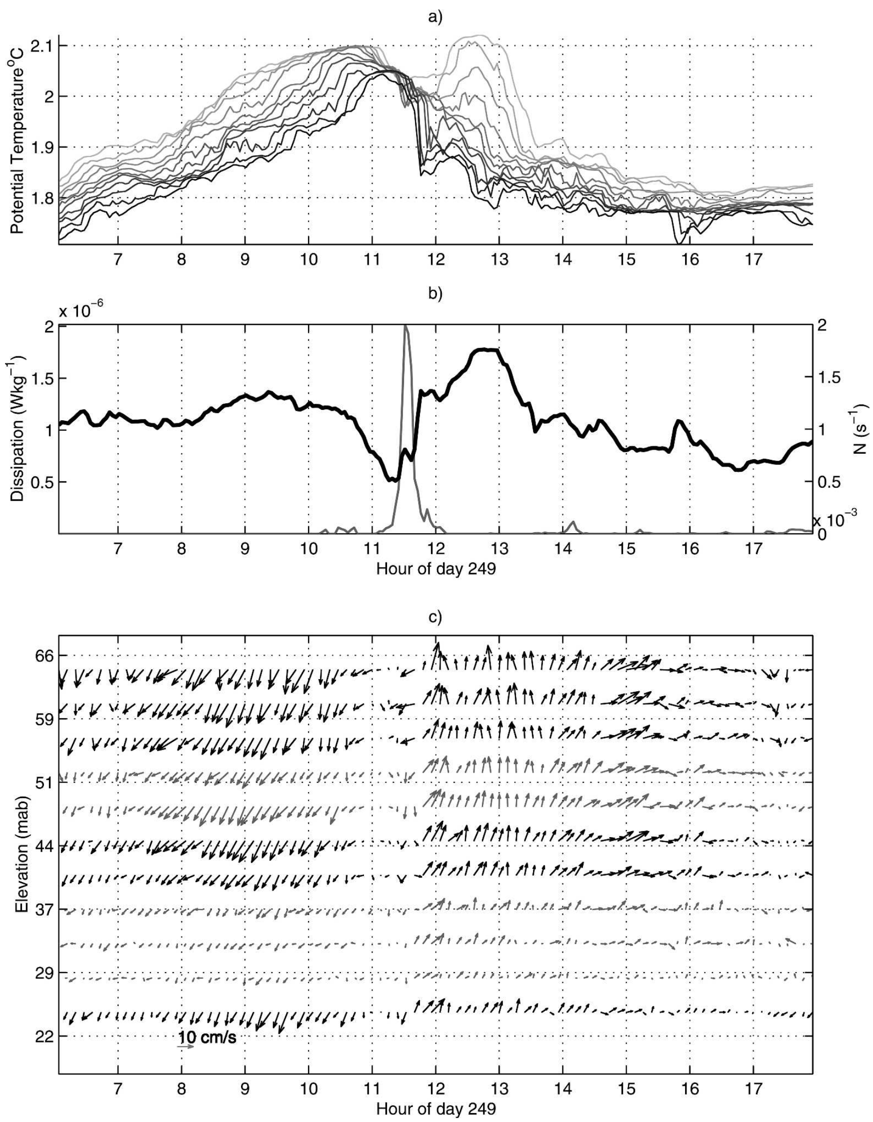

FIG. 8. As in Fig. 7 but for day 249, showing an overturn during a different phase of the tide.

separation between boundary shear and turbulent shear. Then N is computed, averaged over the same range as the ADCP and also over the full range of the thermistors (27–220 mab).

Representative downslope flow mixing events (Fig. 14) occur during each semidiurnal cycle near the time of maximum downslope flow. Flow reversal mixing events are absent during the time period. Downslope flow mixing occurs when the stratification is at a minimum, or equivalently the strain is a maximum, over the tidal cycle. Tidal current shear tends to peak twice during the cycle at both upslope and downslope flow (Figs. 14b and 14c); however, the combination of high shear and strain during the downslope phase results in an inverse Richardson number highly correlated with the dissipation events (Figs. 14b and 14d). The results are similar using different depth ranges for computing N (i.e., 20 versus 200 m). Figure 14c shows the results using N averaged over 200 m because it is less noisy than that based on a 20-m average. We conclude that downslope flow mixing events are the result of shear instability.

At other time periods, flow reversal mixing events are dominant and noticeable downslope flow events are absent (Fig. 15). Strong flow reversal mixing events occur every other semidiurnal cycle. There are also other periods (not shown) when moderate flow reversal events occur at every semidiurnal cycle. In sharp contrast to downslope flow mixing, flow reversal mixing events do not coincide with elevated shear or elevated

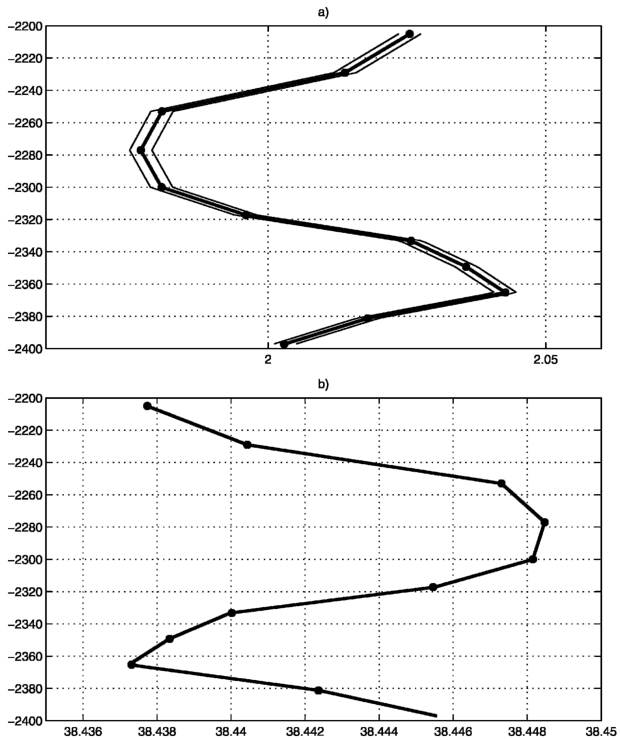

FIG. 9. (a) Vertical profile at day 249, hour 11.5 (Fig. 8) of measured absolute temperature after removing long-term bias. Solid circles indicate depth locations of the instruments. Thin lines represent the measurement plus or minus the nominal accuracy of the instruments. (b) Inferred potential density (-1000 kg m^{-3}).

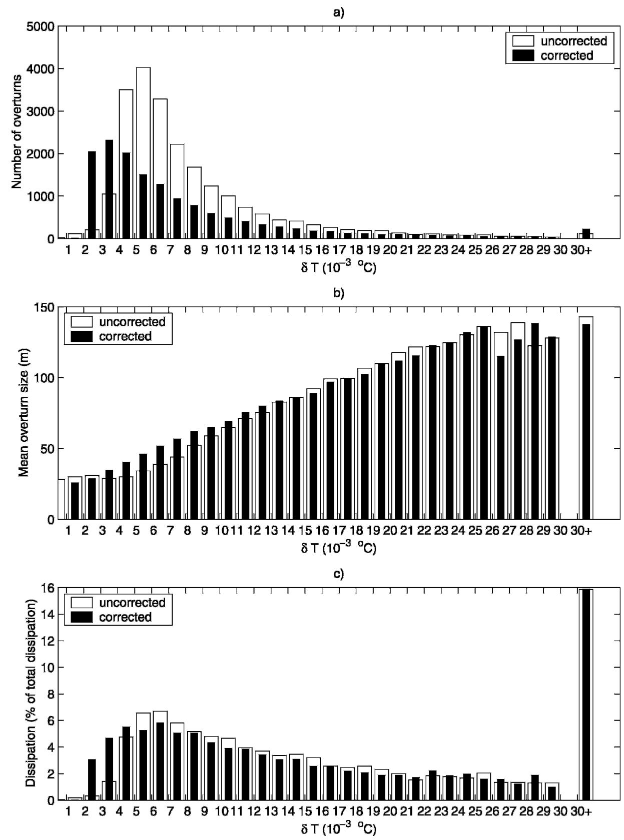

FIG. 10. (a) The distribution of the number of overturns, before and after the temperature correction, as a function of the observed temperature difference across the depths of the overturn. (b) The distribution of overturn size as a function of the temperature difference across the overturn. (c) The distribution of the percentage of the total dissipation contributed by the overturns as a function of the temperature difference across the overturn.

inverse Richardson number (Figs. 15c and 15d). Similar results are obtained using N averaged over the common 20-m depth range as shear, and also using shear and strain computed over 10-m spacings. Stratification minima occur during the events at a phase of the tidal cycle when the stratification would otherwise be increasing (Fig. 15b). The stratification begins to decrease approximately one hour before the main overturning event. This increased strain occurs because of a phase lag of the temperature signal with depth. Inspection of the temperature record for a typical event (Fig. 15a) shows that the isotherms begin to converge prior to mixing because temperatures decrease in the upper water column (150–220 mab) one hour before that in the lower water column (27–75 mab). In the lower water column, the measured currents and temperature are consistent in that temperatures increase during downslope flows. We do not have reliable current measurements to confirm that in the upper water column the early temperature decrease is due to a change to upslope currents.

The poor relationship between flow reversal mixing events and shear or Richardson number may be due to the lack of reliable observations above 65 mab. For example, a shear instability occurring above 65 mab may create an overturn that is advected into the sample range. We believe this is unlikely, however, because the event is characterized by a strong temperature decrease suggestive of a tidal bore. Mixing of warmer waters above the mooring would not result in the generation of waters dense enough to impact the mooring in the sense of a gravity current. Furthermore, the background currents are near zero or directed upslope (i.e., at flow reversal or shortly thereafter). The character of the temperature signal strongly suggests that cold water downslope of the mooring has been uplifted above the mooring, resulting in the instability. Levine and Boyd (2006) also observed mixing associated with the semidiurnal tide to occur at two distinct phases on the north side of Kaena Ridge at 1500-m depth. In their case, overturns near 100 mab occur at 180° out of phase with overturns near 300 mab, both related to enhanced

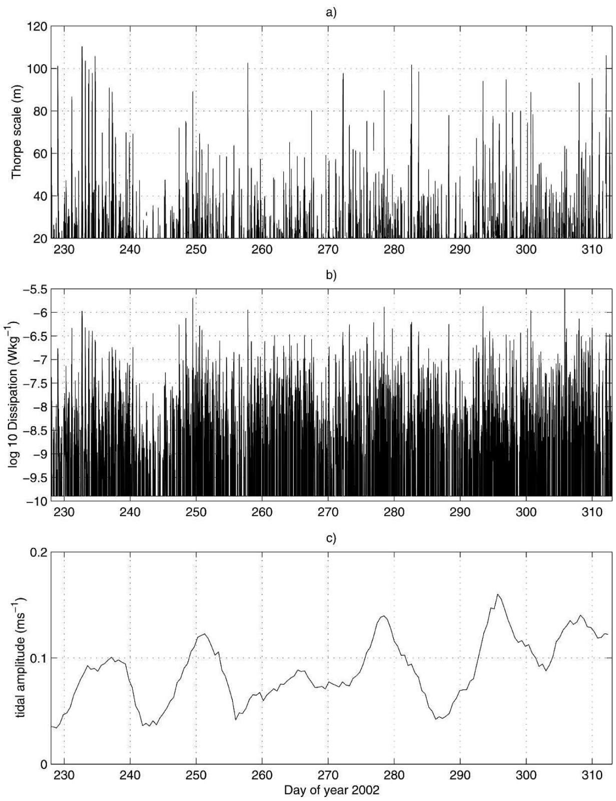

FIG. 11. (a) The estimated Thorpe scale (L_T), (b) dissipation (ϵ), and (c) the measured semidiurnal tidal amplitude using horizontal currents at 65 mab.

strain. Our observations differ in that we see overturns at two tidal phases, but in the same depth range.

For both mixing types, strain appears to be an important precursor to overturning. For downslope flow mixing, overturns occur during the maximum strain over the semidiurnal tidal cycle (Figs. 12 and 14). For flow reversal mixing, overturns occur during a secondary strain maximum that is out of phase with the semidiurnal cycle. Over the entire dataset, the correlation between the strain and dissipation is insignificant (0.19); however, when calculated for a subrecord when downslope flow mixing is dominant (the 3 days shown in Fig. 14), this correlation improves (0.45). For subrecords of similar length, at times when flow reversal mixing is dominant, the correlation between the strain and dissipation does not exceed 0.2. Tidal current shear, at least over the measured depth range, is not significantly correlated with dissipation, even over short periods when only one mixing type is observed (Figs. 14 and 15). Combining the effects of shear and strain, in the form of an inverse Richardson number, does not improve the correlations obtained using strain alone, which again highlights the primary importance of strain for downslope flow events, and further discounts shear instability as a mechanism for flow reversal events.

6. Obliquely propagating internal tides and mixing

Gemmrich and van Haren (2001) documented the occurrence of thermal fronts near the bottom boundary in ~850-m depth along the Bay of Biscay continental slope. They describe abrupt temperature change, linked to the presence of an internal tide beam propagating downward at an oblique angle relative to the slope. Gemmrich and van Haren hypothesized that the obliquely propagating internal tide results in a variation of tidal phase along isobaths, particularly if the internal tide is in the form of a narrow beam. The variable phase of the tidal currents can advect cold water upslope above warm water once per tidal cycle, creating sharp thermal fronts and convective instability. The oblique propagation angle is crucial; an internal tide propagating directly downslope would not generate such unstable fronts. Gemmrich and van Haren observed sharp temperature drops associated with the collapse and/or passage of these fronts. In contrast to the studies of the reflection of internal tides normally incident on a sloping boundary (Nash et al. 2004; Legg and Adcroft 2003), the mechanism identified by Gemmrich and van Haren (2001) relies on downgoing internal tides that propagate obliquely along the slope.

Similarities between the Bay of Biscay and the Kaena Ridge observations suggest that this mechanism may explain the mixing events documented here as "flow reversal mixing." First, for both experiment sites, the observations were made over a supercritical slope for the semidiurnal tide, which allows a tidal beam generated at a ridge crest or shelf break to propagate downward without reflection. Such a beam would propagate farther from the slope with increasing depth; however, Gemmrich and van Haren (2001) describe how obliquely propagating waves still can intersect the slope. This is apparently also the case at the Kaena Ridge: The observed tidal currents are oriented at an angle relative to the slope (Fig. 12), consistent with a tidal beam with an oblique propagation azimuth. Following Gemmrich and van Haren (2001), this could lead to the generation of fronts with an angle φ between 54° and 80° relative to the isobaths ($N = 1 \times 10^{-6}$ s^{-2}, the topographic slope $\alpha = 18.6°$, the M_2 vertical propagation angle is 7.5°, and the angle between the isobath and the bottom projection of the group velocity vector is between 40° and 80°). During the first spring–neap cycle, when flow reversal mixing events are not detected, the current ellipse is more circularly polarized

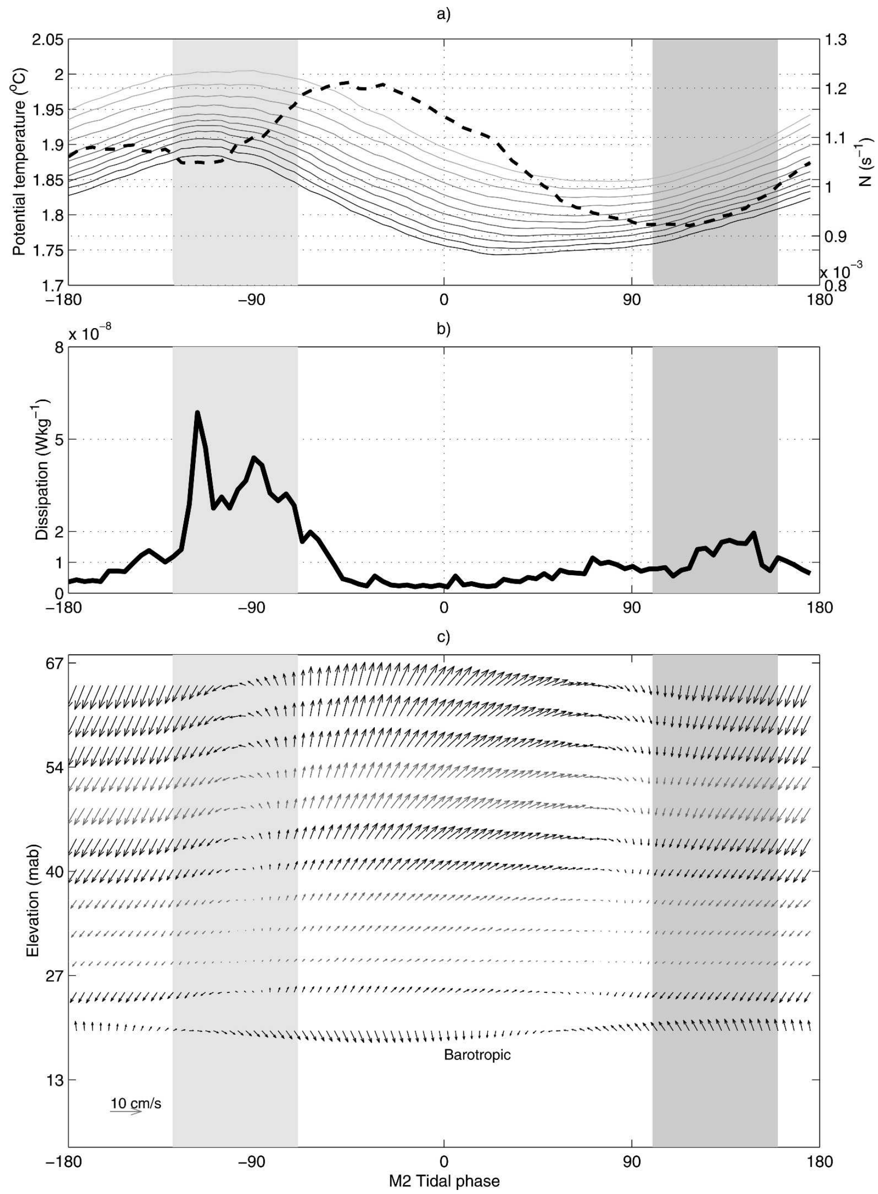

FIG. 12. A composite semidiurnal tidal cycle, obtained using ensemble phase averages over the entire time series, of (a) potential temperature recorded at 27, 43, 59, 75, 91, 107, 124, 147, 171, 195, and 220 mab, with darker lines correpsonding to smaller elevations above the bottom, depth-averaged buoyancy frequency (27–220 mab, dashed black line); (b) estimated dissipation [ϵ, Eq. (3)]; and (c) horizontal currents, rotated so that across-slope velocity is vertical. Depth bins with suspect sidelobe contamination are shown in gray. Estimates of the barotropic current [TPXO (Egbert 1997)] are included. Shaded areas indicate phases of intense mixing associated with downslope flow (dark) and flow reversal (light).

than during the subsequent cycles (Fig. 13b). It appears that a circular current ellipse, as opposed to a more unidirectional flow, is not conducive to this overturning mechanism.

Second, the temperature data from the Bay of Biscay and the Kaena Ridge bear a striking resemblance [our Fig. 8 and Fig. 4 in Gemmrich and van Haren (2001)]. The temperature drops sharply at the time of flow reversal from downslope to upslope, which Gemmrich and van Haren characterized as a passing thermal front. The similarities are particularly striking near the bottom [the Gemmrich and van Haren (2001) observations were all below 50 mab]. Higher in the water column ($\geq$100 mab), above the elevations sampled in the Bay

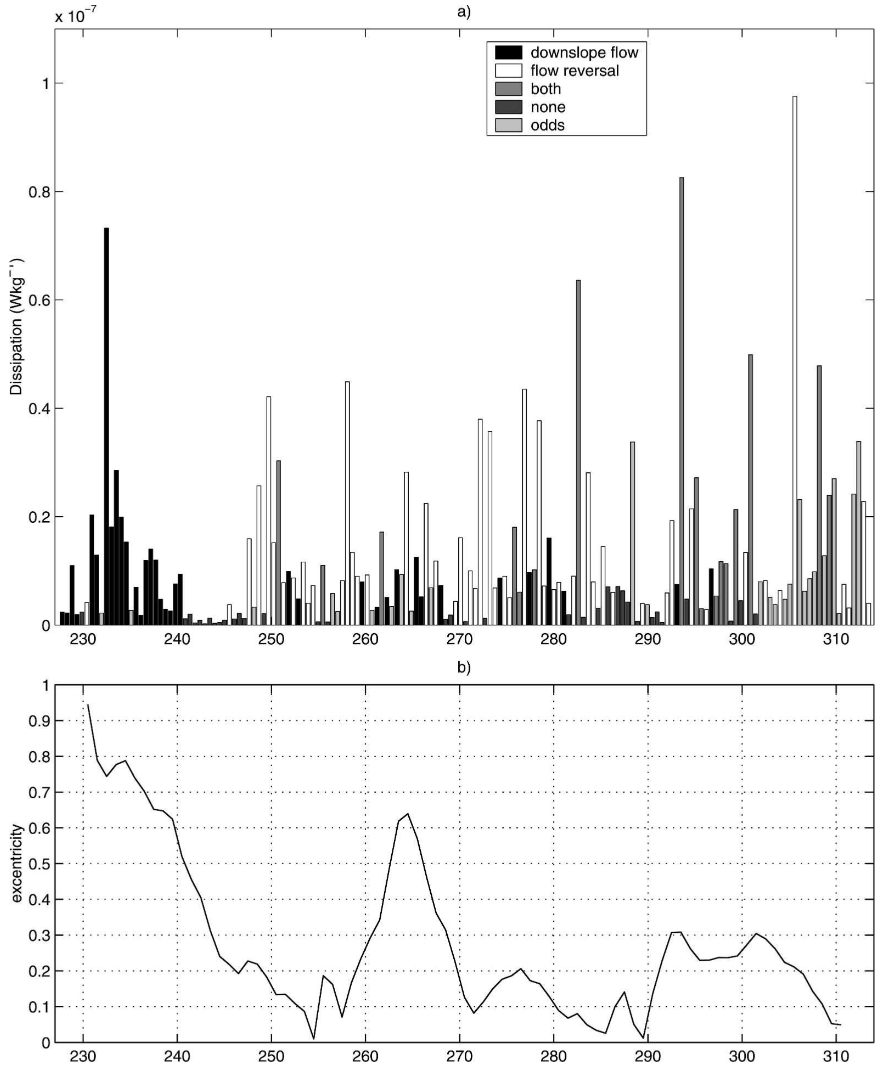

FIG. 13. (a) Dissipation (ϵ), averaged over a semidiurnal cycle, is classified in terms of the dominant mixing types that occur during the cycle. (b) The eccentricity of the semidiurnal current ellipse, quantified as the ratio of the minor over the major axis current amplitude. Ellipse amplitudes are obtained from a harmonic analysis of seven days of subrecords.

of Biscay, we see evidence for strong restratification following the front passage.

Third, tidally driven convection is an attractive mechanism for flow reversal events, given that tidal current and current shears are weak during this phase of the tide. Enhanced strain, which is observed preceding mixing events (Fig. 8), can also be a signature of a developing convective instability rather than a shear instability.

Last, the dependence of this mechanism on the location of the internal tide beam relative to the mooring (Fig. 6 in Gemmrich and van Haren 2001) can also explain the intermittent nature of the observed mixing events. At our Kaena Ridge site, low dissipation is associated with low tidal amplitude, but high tidal amplitude is not always associated with strong dissipation (Fig. 11). Our analysis has focused on the relationship of mixing events to the measured tidal currents. We emphasize that the measured tide is dominated by the baroclinic component at the mooring location (Fig. 12c). The observed increase in amplitude of the semidiurnal currents (Fig. 11c) and the change in eccentricity over the duration of the experiment (Fig. 13b) presumably are attributed to changes in the internal tide. Low-frequency currents and changes in stratification higher in the water column, between the mooring location and the generation site near the ridge top, can cause temporal changes in amplitude, phase, position, or direc-

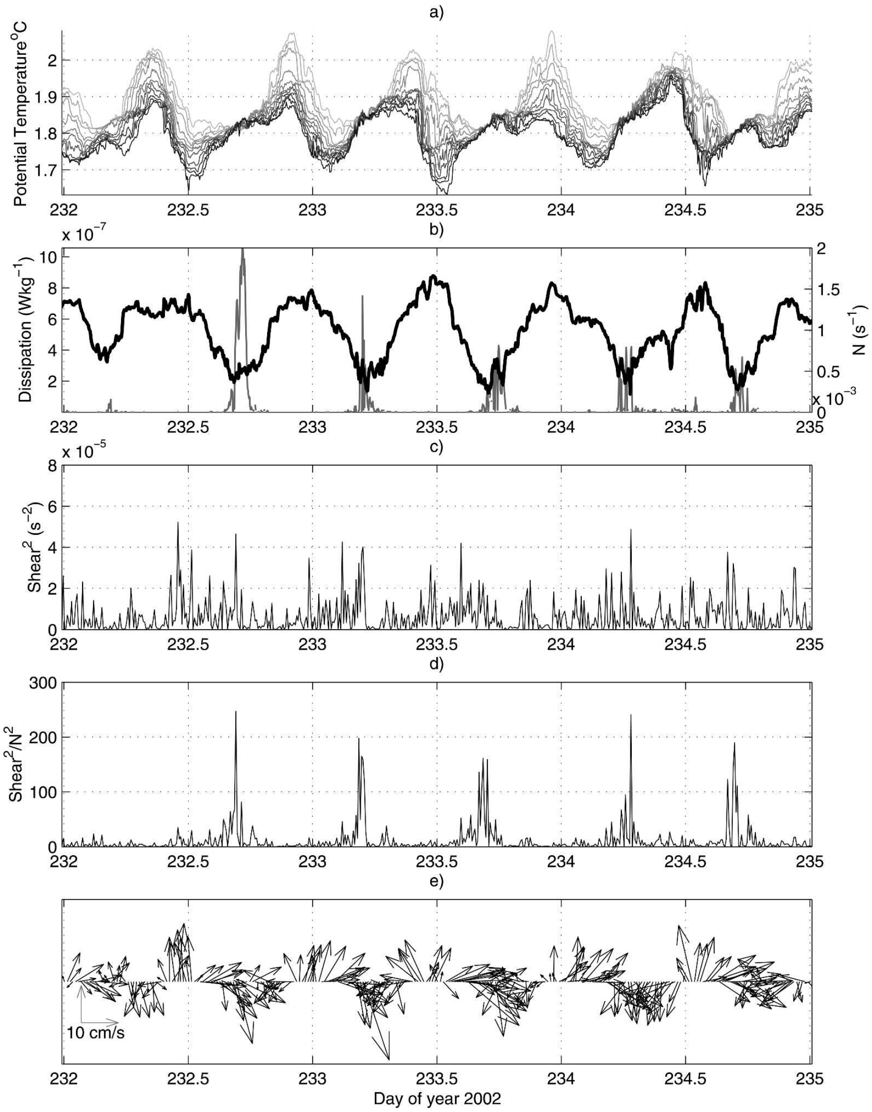

FIG. 14. Downslope flow mixing events in 3-day time series of (a) potential temperature, (b) depth-averaged buoyancy frequency N (27–220 mab, thick black line) and estimated dissipation (thin gray line), (c) square of the horizontal current shear (from 41 to 65 mab), (d) inverse Richardson number (from shear and N above), and (e) the horizontal velocity (at 65 mab).

tion of the internal tide, which apparently influence the level of convective mixing observed at the fixed moored location (Fig. 13a).

7. Summary and discussion

In this field experiment, we find that the semidiurnal tide dominates the current and temperature variability above the steep flanks of the Kaena Ridge. In particular, near-inertial wave energy, diurnal tides, and subinertial currents, which might contribute to near boundary mixing due to bottom drag, are all much weaker than the semidiurnal tide. The predominance of the semidiurnal tide and lack of diurnal tide energy are consistent with their respective predicted ray paths from the model simulations of Merrifield and Holloway (2002). Barotropic-to-baroclinic tidal conversion near the top of Kaena Ridge results in downward-propagating tidal beams that are the primary source of mechanical energy for the ridge.

Overturns and the implied associated mixing and dissipation occur predominantly at two phases of the measured semidiurnal tidal cycle: when flows are near maximum in the downslope direction and at the flow reversal prior to upslope flow, at maximum downward isopycnal displacements. The mechanism causing the

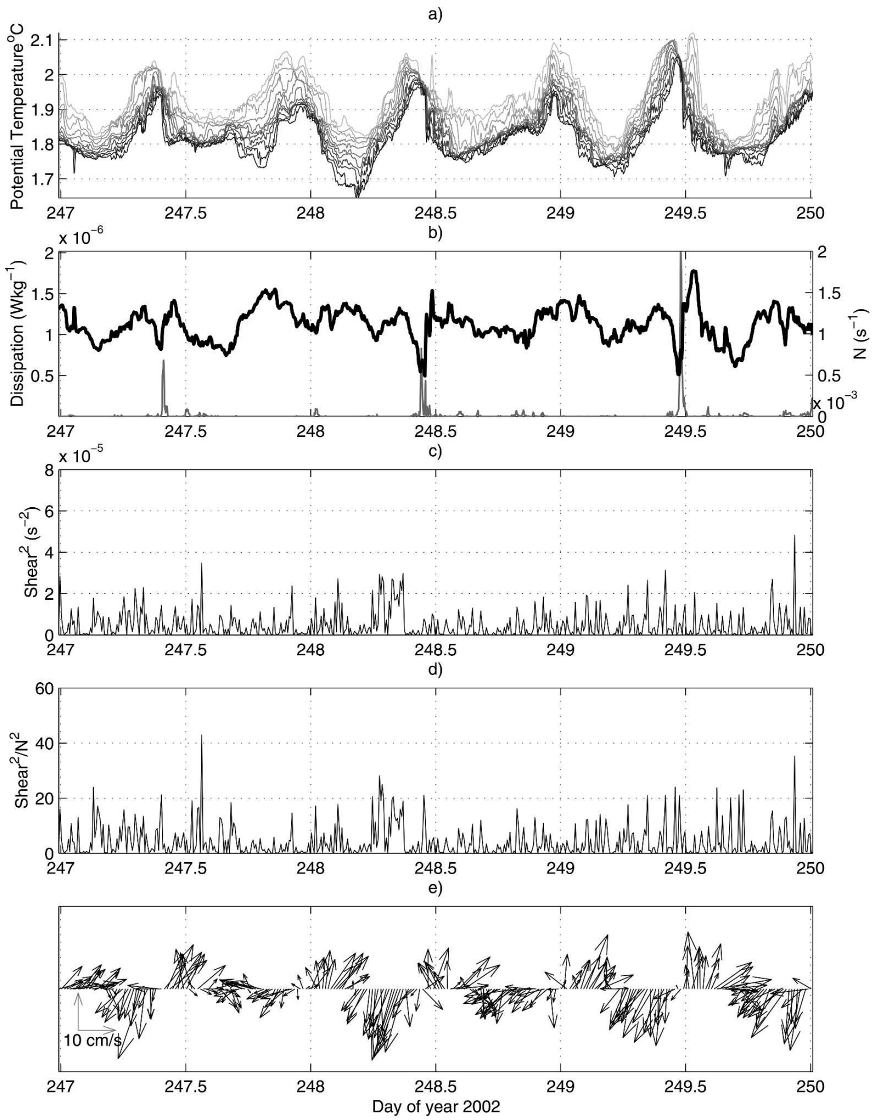

FIG. 15. As in Fig. 14 but for a period of flow reversal mixing events.

downslope flow mixing events appears to be a shear instability, triggered primarily by high strain, occurring when stratification is minimum over the tidal cycle. Levine and Boyd (2006) find a similar relationship between mixing events and strain at a shallower depth on the ridge. Flow reversal mixing occurs during high-strain conditions that do not coincide with the tidal strain maximum. These events appear unrelated to shear and the associated dissipation is poorly correlated with the inverse Richardson number, suggesting that shear instability is not the primary generation mechanism. Based on similarities with observations made by Gemmrich and van Haren (2001) in the Bay of Biscay, we suspect that the flow reversal mixing events are convectively driven. In this scenario, mixing develops because of the oblique propagation angle of the downward-propagating internal tide relative to the slope. This leads to the advection of cold water above warm water along the slope, the generation of a sharp thermal front, and eventually to statically unstable conditions and overturning. Evidence supporting this hypothesis includes the observed orientation of the internal tide relative to the slope, the abrupt temperature decrease associated with the overturn, and the poor correspondence with tidal shear. The enhanced strain preceding these events may result from the development of a statically unstable patch.

Ultimately, we seek a tidal mixing parameterization that can be incorporated into regional numerical models so that estimates of deep mixing can be extrapolated to the entire ridge system, as well as to other locations. We might expect that the mixing associated with the tide would have a high predictability. Although the internal tide provides most of the mechanical energy at this site, a few tidal consituents explain a significant fraction of the observed variability, presumably due to the proximity of the mooring to the generation site(s). Although both mixing events are linked to the tide, neither is as predictable as the tide itself. Downslope flow mixing events exhibit a visual correspondence with inverse Richardson number; however, at best the correlation is only 0.4. This may be due to limitations in our current measurements, which only resolved shear over a small fraction of the overturning depth range. We believe that a traditional mixing parametrization based on tidal strain and shear may be useful to explain downslope flow mixing.

If flow reversal mixing is caused by convective instabilities in the manner described by Gemmrich and van Haren (2001), a mixing parametrization is more complicated. Predictability would depend on the orientation of the internal tide relative to the topography, which in turn requires detailed knowledge of how changes in the background stratification and currents affect the generation and propagation of the internal tide. Small changes in the propagation azimuth of the internal tide presumably would lead to significant changes in mixing.

In the context of the other HOME observations at Kaena Ridge, we find good agreement between our inferred dissipation rates based on Thorpe scales and direct microstructure measurements. Our estimated time-averaged dissipation is 1.2×10^{-8} W kg^{-1} but can reach up to 10^{-6} W kg^{-1}. The corresponding time-averaged eddy diffusity is 2×10^{-3} m^2 s^{-1}. For comparison, Levine and Boyd (2006) and Klymak et al. (2006) found comparable average dissipation values of 2×10^{-8} W kg^{-1} at the 1450-m isobath and 4×10^{-9} W kg^{-1} at 3000 m, respectively. The microstructure measurements suggest that mixing rates are enhanced 100–200 mab near the bottom (Klymak et al. 2006). Given the sporadic and eventlike nature of the mixing, the value of continuous sampling over time for estimating mixing is highlighted by our observations. It is remarkable that the two methods of estimating mixing, microstructure profiles versus overturns from continuous temperature time series, give such consistent results.

Rainville and Pinkel (2006), using data obtained on the ridge crest from Research Platform (R/P) *Floating Instrument Platform* (*FLIP*) (Fig. 1), found enhanced strain at diurnal, not semidiurnal, time scales. They conclude that parametric subharmonic instabilities (PSIs) are an important pathway from the semidiurnal tide to small scales. Here we find enhanced shear and strain only at semidiurnal frequencies. This suggests that PSIs may be an important mechanism over the ridge (Rainville and Pinkel 2006; Carter and Gregg 2006) but apparently not over the deep ridge flanks. We note that our study site is below the main thermocline, within a depth range that has been a focus of abyssal mixing studies (Munk and Wunsch 1998). The preliminary HOME results from Kaena Ridge encourage speculations that tidally driven mixing mechanisms may differ above and below the main thermocline.

These results are not necessarily specific to Hawaii, or even ridge topographies. Internal tides are generated at many continental shelf breaks, and, combined with supercritical or critical continental slopes, downgoing tidal beams are likely to interact with the topography. The relative importance of tidally driven shear instability and convective mixing, as described by Gemmrich and van Haren (2001), remains to be determined. Given the large fraction of continental slope worldwide where downgoing tidal beams are potentially present, we speculate that these beams may account for a significant fraction of the mixing occurring at deep oceanic boundaries. This mechanism has received less attention than the critical reflections of incident internal tides.

Future work will include an analysis of mooring data from a later deployment on the north flank of the ridge, as well as 12-h repeat surveys of the bottom boundary layer made using CTD and a lowered ADCP. Based on these analyses and comparisons with numerical simulations of the internal tide, we hope to gain a better understanding of flow reversal mixing along the deep flanks of the Hawaiian Ridge.

Acknowledgments. The successful deployment and recovery of our HOME moorings from the R/V *Wecoma* under sometimes adverse conditions was achieved in large part because of the skill and knowledge of Captain Dan Arnsdorf, Assistant Engineer Duane Leafdahl, Marine Technician Daryl Swensen, and the entire crew. We also thank Walt Waldorf for his expert assistance in deploying and recovering the moorings. Eric Firing provided helpful advice in analyzing the ADCP data. Discussions with Murray Levine, Tim Boyd, and the other HOME investigators are greatly appreciated. The suggestions from two anonymous reviewers significantly improved the presentation and interpretation of the results. We appreciate the support of the National Science Foundation through Grants OCE-9819533 and OCE9819519, and the efforts of program manager Eric Itsweire in facilitating the HOME project.

REFERENCES

Armi, L., 1978: Some evidence for boundary mixing in the deep ocean. *J. Geophys. Res.,* **83,** 1971–1979.

——, 1979: Reply to comments by C. Garrett. *J. Geophys. Res.,* **84,** 5097–5098.

Budeus, G., and W. Schneider, 1998: In-situ temperature calibration: A remark on instruments and methods. *International WOCE Newsletter,* No. 30, International Project Office, Southampton, United Kingdom, 16–18.

Carter, G. S., and M. C. Gregg, 2006: Persistent near-diurnal internal waves observed above a site of M_2 barotropic-to-baroclinic conversion. *J. Phys. Oceanogr.,* **36,** 1136–1147.

Dillon, T. M., 1982: Vertical overturns: A comparison of Thorpe and Ozmidov length scales. *J. Geophys. Res.,* **87,** 9601–9613.

Dushaw, B. D., B. M. Howe, B. D. Cornuelle, P. F. Worcester, and D. S. Luther, 1995: Barotropic and baroclinic tides in the central North Pacific Ocean determined from long-range reciprocal acoustic transmissions. *J. Phys. Oceanogr.,* **25,** 631–647.

Egbert, G., 1997: Tidal data inversion: Interpolation and inference. *Progress in Oceanography,* Vol. 40, Pergamon, 53–80.

——, and R. D. Ray, 2000: Significant dissipation of tidal energy in the deep ocean inferred from satellite altimeter data. *Nature,* **405,** 775–778.

Eriksen, C., 1998: Internal wave reflection and mixing at Fieberling Guyot. *J. Geophys. Res.,* **103,** 2977–2994.

Ferron, B., H. Mercier, K. Speer, A. Gargett, and K. Polzin, 1998: Mixing in the Romanche fracture zone. *J. Phys. Oceanogr.,* **28,** 1929–1945.

Finnigan, T., D. Luther, and R. Lukas, 2002: Observations of enhanced diapycnal mixing near the Hawaiian Ridge. *J. Phys. Oceanogr.,* **32,** 2988–3002.

Foreman, M. G. G., 1978: Manual for tidal currents analysis and prediction. Institute of Ocean Sciences Pacific Marine Science Rep. 78-6, 57 pp.

Garrett, C., 1991: Marginal mixing theories. *Atmos.–Ocean,* **29,** 313–339.

Gemmrich, J. R., and H. van Haren, 2001: Thermal fronts generated by internal waves propagating obliquely along the continental slope. *J. Phys. Oceanogr.,* **31,** 649–655.

Gregg, M. C., 1991: The study of mixing in the ocean: A brief history. *Oceanography,* **4,** 39–45.

Gross, T. F., A. J. Williams III, and W. D. Grant, 1986: Long-term in situ calculations of kinetic energy and Reynolds stress in a deep sea boundary layer. *J. Geophys. Res.,* **91,** 8461–8469.

Hasumi, H., and N. Suginohara, 1999: Effects of locally enhanced vertical diffusivity over rough bathymetry on the World Ocean circulation. *J. Geophys. Res.,* **104,** 23 637–23 374.

Klymak, J. M., and Coauthors, 2006: An estimate of tidal energy lost to turbulence at the Hawaiian Ridge. *J. Phys. Oceanogr.,* **36,** 1148–1164.

Kunze, E., and J. M. Toole, 1997: Tidally driven vorticity, diurnal shear, and turbulence atop Fieberling Seamount. *J. Phys. Oceanogr.,* **27,** 2663–2693.

Lee, C. M., E. Kunze, T. Sanford, J. D. Nash, M. A. Merrifield, and P. E. Holloway, 2006: Internal tides and turbulence along the 3000-m isobath of the Hawaiian Ridge. *J. Phys. Oceanogr.,* **36,** 1165–1183.

Legg, S., and A. Adcroft, 2003: Internal wave breaking at concave and convex continental slopes. *J. Phys. Oceanogr.,* **33,** 2224–2246.

Levine, M. D., and T. J. Boyd, 2006: Tidally forced internal waves and overturns observed on a slope: Results from HOME. *J. Phys. Oceanogr.,* **36,** 1184–1201.

Lien, R.-C., and M. C. Gregg, 2001: Observations of turbulence in a tidal beam and across a coastal ridge. *J. Geophys. Res.,* **106,** 4575–4592.

Lukas, R., F. Santiago-Mandujano, F. Bingham, and A. Mantyla, 2000: Cold bottom water events observed in the Hawaii Ocean Time-Series: Implications for vertical mixing. *Deep-Sea Res.,* **48,** 995–1021.

Merrifield, M. A., and P. E. Holloway, 2002: Model estimates of M2 internal tide energetics at the Hawaiian Ridge. *J. Geophys. Res.,* **107,** 3179, doi:10.1029/2001JC000996.

Munk, W. H., 1966: Abyssal recipes. *Deep-Sea Res.,* **13,** 207–230.

——, and C. Wunsch, 1998: Abyssal recipes II: Energetics of tidal and wind mixing. *Deep-Sea Res.,* **45,** 1978–2010.

Nash, J. D., E. Kunze, J. M. Toole, and R. W. Schmitt, 2004: Internal tide reflection and turbulent mixing on the continental slope. *J. Phys. Oceanogr.,* **34,** 1117–1134.

——, ——, C. M. Lee, and T. B. Sanford, 2006: Structure of the baroclinic tide generated at Kaena Ridge, Hawaii. *J. Phys. Oceanogr.,* **36,** 1123–1135.

New, A. L., and R. D. Pingree, 1990: Evidence for internal tidal mixing near the shelf break in the Bay of Biscay. *Deep-Sea Res.,* **37,** 1783–1804.

Osborn, T. R., 1980: Estimates of the local rate of vertical diffusion from dissipation measurements. *J. Phys. Oceanogr.,* **10,** 83–89.

Ozmidov, R. V., 1965: On the turbulent exchange in a stably stratified ocean. *Atmos. Oceanic Phys.,* **8,** 853–860.

Phillips, O. M., J. Shyu, and H. Salmun, 1986: An experiment on boundary mixing: Mean circulation and transport rates. *J. Fluid Mech.,* **173,** 473–499.

Polzin, K. L., J. M. Toole, J. R. Ledwell, and R. W. Schmitt, 1997: Spatial variability of turbulent mixing in the abyssal ocean. *Science,* **276,** 93–96.

Rahmstorf, S., 2003: The current climate. *Nature,* **421,** 699.

Rainville, L., and R. Pinkel, 2006: Baroclinic energy flux at the Hawaiian Ridge: Observations from the R/P *FLIP. J. Phys. Oceanogr.*, **36,** 1104–1122.

Ray, R. D., and G. T. Mitchum, 1996: Surface manifestation of internal tides generated near Hawaii. *Geophys. Res. Lett.,* **23,** 2101–2104.

Samelson, R. M., 1998: Large-scale circulation with locally enhanced vertical mixing. *J. Phys. Oceanogr.,* **28,** 712–726.

Simmons, H. L., S. Jayne, L. S. Laurent, and A. Weaver, 2004: Tidally driven mixing in a numerical model of the ocean general circulation. *Ocean Modell.,* **6,** 245–263.

Thorpe, S. A., 1977: Turbulence and mixing in a Scottish Loch. *Philos. Trans. Roy. Soc. London,* **286,** 125–181.

——, 1999: $75 + 25 = 99 \pm 1$, or some of what we still don't know: Wave groups and boundary processes. *Dynamics of Oceanic Internal Gravity Waves: Proc. 'Aha Huliko'a Hawaiian Winter Workshop,* Honolulu, HI, University of Hawaii at Manoa, 129–131.

Toole, J. M., R. W. Schmitt, K. L. Polzin, and E. Kunze, 1997: Near-boundary mixing above the flanks of a midlatitude seamount. *J. Geophys. Res.,* **102,** 947–959.

Wunsch, C., 2000: Moon, tides and climate. *Nature,* **405,** 743–744.